JOURNAL OF SPACECRAFT AND ROCKETS
Vol. 48, No. 3, May–June 2011

Simulating Stardust Earth Reentry with Radiation Heat Transfer

J. S. Shang*
Wright State University, Dayton, Ohio 45435
and
S. T. Surzhikov†
Russian Academy of Sciences, 119526, Moscow, Russia

DOI: 10.2514/1.52029

A multigroup spectral method is integrated into an interdisciplinary formulation for nonequilibrium radiative hypersonic flows. The developed simulation capability has been successfully applied to study the Stardust capsule Earth reentry via an axisymmetric approximation. The predicted total heat transfer rates at different stages of reentry achieve a reasonable agreement with results in literature. The computational results reveal a close correlation between the relaxation of vibrational excitations and diffusive heat transfer in the wake, as well as a diminished radiative intensity and a shifted emission spectrum in the shock layer toward the lower-frequency domain from the earlier to the later stages of the reentry.

Nomenclature

$\mathbf{B}$	=	magnetic flux density, Wb/m
c_v	=	specific heat at constant volume, J/kg K
$\mathbf{E}$	=	electric field strength, V/cm
e	=	internal energy, J/kg
h	=	enthalpy per unit volume, J/kg
$\mathbf{I}$	=	identity matrix
$\mathbf{J}$	=	electric current density, A/m^2
$\mathbf{J}_\omega$	=	spectral intensity of radiation, J/m^2 sHz
$\mathbf{j}_w$	=	spectral emission coefficient, J/msHz
$\mathbf{r}$	=	position vector, m
p	=	static pressure, N/m^2
Q	=	rate of internal energy transfer, W/kg
$\mathbf{q}$	=	rate of heat transfer, W/m^2
T	=	temperature, K
t	=	time, s
$\mathbf{u}$	=	velocity, m/s
w	=	production of species, number of mole
X	=	molar fraction of species
κ	=	thermal conductivity, J/msK
κ_w	=	spectral absorption coefficient, rad/m
ρ	=	density, kg/m^3
$\boldsymbol{\tau}$	=	shear stress tensor, N/m^2
Ω	=	solid angle of radiation, rad
ω	=	spectral frequency of radiation, Hz

Subscripts

i	=	different chemical species
vt, et	=	interaction of vibration–translation, electron–translation
Σ	=	sum of energy transfer between internal degrees of freedom

Presented as Paper 2010-4455 at the 40th Fluid Dynamics Conference, Chicago, IL, 28 June–1 July 2010; received 17 August 2010; revision received 19 January 2011; accepted for publication 31 January 2011.

*Research Professor, Department of Mechanical and Materials Engineering; joseph.shang@wright.edu. Fellow AIAA.

†Professor, A. Ishlinskiy Institute for Problems in Mechanics; Deputy Director, and Head of Radiative Gasdynamics Laboratory. Associate Fellow AIAA.

Introduction

THE heat transfer rate of the reentering Stardust sample return capsule in a nonequilibrium, ablative, aerothermodynamic environment was first investigated by Olynick et al. [1] in 1999 and more recently by Park [2]. At the reentry speed in excess of 12.4 km/s, the radiation emanates mostly from the combination of molecular and atomic species [3]. The radiation significantly increases the amount of energy exchanged with its surroundings at a higher entry speed, and the electronic excitation of the high-temperature gas becomes the major mechanism of the radiative energy exchange.

The radiative energy transfer generally associates with the energy states of electronic transition in atoms, molecules, ions, and electron–ion plasma [4]. The high-temperature gas mixture during the Earth reentry is usually electronically excited, and both the discrete and continuous radiative processes occur in the energy spectrum. Therefore, radiation energy transfer for Stardust reentry has wide spectra from infrared to vacuum ultraviolet [2,5]. In modeling the chemical kinetics for Earth reentry, the rate coefficients of all the nonequilibrium ionizations have a limited validation database [2,3,6,7]. The fundamental knowledge shortfall in the ionization process and electron–vibration energy exchange model also severely limits the numerical simulation using direct simulation Monte Carlo method [8,9].

For the conductive–convective heat transfer simulation during Earth reentry, the physical fidelity of electronic chemical kinetic models is not overly critical, as reflected by all benchmark simulations based on LAURA [10] or DPLR [11] and for ablation by Milos and Chen [12] and Chen and Milos [13,14]. Recent investigations by Shang and Surzhikov [15,16], Shang [17], and Surzhikov and Shang [18] have shown that in the absence of an externally applied electromagnetic field, the Lorentz acceleration and Joule heating are insignificant in globally neutral partial ionized plasma. In addition, the major portion of energy transfer to the electronic excitation is still the chemical kinetic process for Stardust reentry: the fastest man-made object. To demonstrate this observation, the governing equation system was reduced by eliminating the electronic energy transfer mechanisms from lower degrees of excitation and was applied to simulate the peak heating condition [15]. The resultant conductive–convective heat transfer rate is within the scattering range of the well-known simulations [1,2]. However, it is critically important to note that the energy transfer to and from the electronic excitation is not ignorable, and it does have a profound

influence on the nonequilibrium chemical reactions, but the uncertainty in the ionization kinetic model must be alleviated for future scientific advancement [15–18].

In the search for a better understanding of the relaxation phenomenon of internal degrees of excitation, a comparative study has been performed on the coupling of the vibration-to-dissociation process in Stardust reentry [15]. Two kinetic models are selected for this purpose: one of the models is the preferential dissociation formulation by Treanor and Marrone [19] and the other is the widely adopted two-temperature model by Park [2,7]. In spite of the fact that these two models have an entirely different origin (the former has a theoretical base, and the latter is by insight and experience), these models generate nearly an identical heat transfer rate on the Stardust capsule at peak heating load [15]. The only meaningful conclusions can be drawn from this result is that the perturbation of dissociation-to-vibration relaxation at the peak heating condition of Stardust entry is relatively insignificant. Nevertheless, the energy exchange at elastic electron–ion collision has recently been modeled using the Coulomb logarithm [6]. The electron impact ionization is also formulated for the electron energy conservation equation [6,20].

At the peak heating condition of the Stardust reentry, the radiation heat transfer rate is 120 W/cm^2 versus the convective–convective heat transfer rate of 839 W/cm^2 [1,2]. In computing radiative heat transfer, a wide range of assumptions for the thermodynamic states of ionized species and the coupling of high-temperature gas dynamics and radiation were adopted [1–3,8,9,21,22]. The most popular approach is derived from the common database of NEQAIR, which is a spectral line-by-line radiative code with one-dimensional energy transport [23]. A direct comparison of numerical simulation with data of Stardust reentry collected from the echelle spectrograph has been carried out by Liu et al. [22]. Their results have replicated the general features and trends of the measured spectra. In the present approach, the absorption and emission coefficients for solving the nonequilibrium radiative intensity equation are derived from the spectra data of the local gas composition and thermodynamic state via the semi-empirical or ab initio approach of quantum mechanics [24,25].

In practical applications, the multigroup, wideband, and narrowband spectrum and the line-by-line integration over a spectrum models of selective radiation heat transfer are commonly used [6,24,25]. A detailed classification of different models, which are used in theory of radiation heat transfer, is given in the work by Surzhikov [25]. All these models use a similar computational algorithm; namely, the investigated spectrum range is divided into finite spectral regions. Within each narrow spectral region, the equation of radiation heat transfer is solved by the frequency-independent spectral coefficients of emission and absorption.

The improved chemical kinetics for ionization and its coupling with the multigroup spectral method for radiation will be the major objective of the present investigation. A sequence of computational simulations of the Stardust along the trajectory of Stardust reentry is conducted first to examine the transition of international energy distribution of the entire flowfield. The corresponding radiative emission and absorption of the electromagnetic wave energy will be delineated with respect to the shifting spectrum of the radiative heat transfer associated with the nonequilibrium thermodynamic state and chemical reactions.

Governing Equations

The coupling of high-temperature gas dynamics and radiative heat transfer has been studied over the past 50 years [4,26]. The emission, absorption, and scattering of a propagating electromagnetic wave occur within the molecular and atomic structure of a gas particle, which is beyond the realm of gas kinetic theory. The essential interaction between the distinct physical phenomena is the chemical composition and the energy state of a gas medium. Therefore, the most convenient approach in addressing the additional energy exchange process is by integrating the radiative heat transfer as a heat source or sink into the global energy conservation equation. Therefore, it is necessary to supplement the energy conservative equation with the equation of spectral intensity for radiation. In view of the drastically different mechanisms and time scales of the convective and radiative processes, the close or loose coupling of gas dynamics and radiation is no longer a critically important issue, except for maintaining computational stability [21–23].

The detailed mechanisms for nonequilibrium reacting gas are developed from chemical and gas kinetic models. The conservation equations in continuum medium can be given as [15–18]

$$\frac{\partial \rho_i}{\partial t} + \nabla \cdot [\rho_i(\mathbf{u} + \mathbf{u}_i)] = \frac{\mathrm{d}w_i}{\mathrm{d}t} \tag{1}$$

$$\frac{\partial \rho u}{\partial t} + \nabla \cdot (\rho \mathbf{u}\mathbf{u} + p\mathbf{I} - \boldsymbol{\tau}) = 0 \tag{2}$$

$$\frac{\partial \rho e}{\partial t} + \nabla \cdot [\rho e \mathbf{u} - \kappa \nabla T + \sum \rho_i \mathbf{u}_i h_i + \mathbf{q}_{\mathrm{rad}} + \mathbf{u} \cdot p\mathbf{I} + \mathbf{u} \cdot \boldsymbol{\tau}] + Q_{\mathrm{vt}} - Q_{\mathrm{et}} = 0 \tag{3}$$

Vibrational energy conservation equations for polyatomic molecular species are

$$\frac{\partial \rho_i e_{iv}}{\partial t} + \nabla \cdot [\rho_i(\mathbf{u} + \mathbf{u}_i)e_{iv} + \mathbf{q}_{iv})] = e_{iv}\frac{\mathrm{d}w_i}{\mathrm{d}t} + Q_{v,\Sigma} \tag{4}$$

From the carefully examination of the nonequilibrium ionized air species; the sum of number densities of the positive charged components N_2^+, O_2^+, NO^+, N^+, and O^+ is identical to that of the free electron within the shock layer and at the vehicle surface [15–18]. It is not surprising, because this is the classical behavior of plasma. In the absence of an externally applied electromagnetic field, the electrostatic force $\rho_e\mathbf{E}$, Lorentz acceleration $\mathbf{J} \times \mathbf{B}$, and Joule heating $\mathbf{E} \cdot \mathbf{J}$ are insignificant. As a consequence, the effect of the electromagnetic force and the work done to the gas mixture is also extremely limited and these terms are eliminated from the electronic conservation energy equation. The simplified electronic energy conservation equations based on physics is given as

$$\frac{\partial \rho_i e_e}{\partial t} + \nabla \cdot [\rho_i(\mathbf{u} + \mathbf{u}_i)e_e + \mathbf{u} \cdot p_e\mathbf{I} + \mathbf{q}_e)] = e_e\frac{\mathrm{d}w_i}{\mathrm{d}t} + Q_{e,\Sigma} \tag{5}$$

However, the electrically conducting medium has a pronounced effect to electromagnetic wave propagation known as the communication blackout. This phenomenon is governed by the relative frequencies of the incident wave and the plasma.

The net energy transfers between translational, vibrational, and electronic excitations that appears in Eqs. (4–6) are designated as Q_{vt}, Q_{et}, $Q_{v,\Sigma}$, and $Q_{e,\Sigma}$, respectively. A wide range of plausible models have been proposed and implemented [3,6,7,20–24].

The preferential dissociation model by Treanor and Marrone [19] is adopted for the energy transfer between electronic and vibrational excitations instead of the two-temperature model by Park [2,7]. The basic idea is that the rate of molecular dissociation can occur preferentially from the higher vibrational quantum levels:

$$Q_{\mathrm{ev}} = \sum_i \bar{\varepsilon}_{\mathrm{vi}}\left(\frac{\mathrm{d}n_i}{\mathrm{d}T}\right); \qquad i \approx \exp\left[\frac{-(D - \nu e_i)}{\kappa T}\right] \tag{6}$$

For the internal energy transfer between electron and neutral species collision, a simple kinetic model has been successfully adopted in computational simulations [6,15–17,20,24]:

$$Q_{\mathrm{et}} = 3378 \times 10^{10} X_e X_t \sqrt{T_e}(T - T_e)\left[1 - \left(1 + \frac{T_e}{T_t^*}\right)^{-1}\right] \tag{7}$$

where the average translational temperature of neutral species is T_t^*. This subject will remain as a sustained research focus for basic research in hypersonic flow into the future.

Table 1 Chemical kinetic rates of the 18-species model of Olynick et al. [1]

		A_f, (cm^3/mol)/s	n_f	E_f, K	A_r, (cm^3/mol)/s	n_r	E_r, K
1	$N_2 + M \leftrightarrow N + N + M$	0.70E + 22	−1.6	0.113E + 06	0.74E + 17	−0.6	0.
2	$O_2 + M \leftrightarrow O + O + M$	0.20E + 22	−1.5	0.598E + 06	0.267E + 17	−0.5	0.
3	$NO + M \leftrightarrow N + O + M$	0.50E + 16	0.0	0.755E + 05	0.258E + 12	1.0	0.
4	$C_2 + M \leftrightarrow C + C + M$	0.37E + 15	0.0	0.690E + 05	0.117E + 11	1.0	0.
5	$CO + M \leftrightarrow C + O + M$	0.23E + 21	−1.0	0.129E + 06	0.130E + 16	0.0	0.
6	$CN + M \leftrightarrow C + N + M$	0.25E + 15	0.0	0.710E + 05	0.857E + 10	1.0	0.
7	$CO_2 + M \leftrightarrow CO + O + M$	0.69E + 22	−1.5	0.633E + 05	0.142E + 17	−0.5	0.
8	$C_3 + M \leftrightarrow C_2 + C + M$	0.63E + 17	−0.5	0.101E + 06	0.523E + 12	0.5	0.160E + 05
9	$H_2 + M \leftrightarrow H + H + M$	0.22E + 15	0.0	0.483E + 05	0.695E + 10	1.0	0.
10	$NO + O \leftrightarrow O_2 + N$	0.84E + 13	0.0	0.195E + 05	0.325E + 14	0.0	0.348E + 04
11	$N_2 + O \leftrightarrow NO + N$	0.64E + 18	−1.0	0.384E + 05	0.132E + 18	−1.0	0.467E + 03
12	$CO + O \leftrightarrow O_2 + C$	0.39E + 14	−0.18	0.692E + 05	0.164E + 14	−0.18	0.
13	$CO_2 + O \leftrightarrow O_2 + CO$	0.21E + 14	0.0	0.278E + 05	0.323E + 13	0.0	0.240E + 05
14	$CO + C \leftrightarrow C_2 + O$	0.20E + 18	−1.0	0.580E + 05	0.356E + 17	−1.0	0.933E + 03
15	$CO + N \leftrightarrow CN + O$	0.10E + 15	0.0	0.386E + 05	0.164E + 14	0.0	0.
16	$N_2 + C \leftrightarrow CN + N$	0.11E + 15	−0.11	0.232E + 05	0.340E + 14	−0.11	0.
17	$CN + O \leftrightarrow NO + C$	0.16E + 14	0.1	0.146E + 05	0.106E + 14	0.1	0.377E + 03
18	$CN + C \leftrightarrow C_2 + N$	0.50E + 14	0.0	0.130E + 05	0.543E + 14	0.0	0.
19	$HCN + H \leftrightarrow CN + H_2$	0.80E + 12	0.017	0.835E + 05	0.564E + 12	0.017	0.930E + 05
20	$C + e- \leftrightarrow C^+ + e - + e-$	0.635E + 16	0.0	0.138E + 06	0.268E + 15	1.0	0.403E + 04
21	$N + e- \leftrightarrow N^+ + e - + e-$	0.508E + 17	0.0	0.121E + 06	0.667E + 15	1.0	0.
22	$O + e- \leftrightarrow O^+ + e - + e-$	0.635E + 16	0.0	0.106E + 06	0.339E + 15	1.0	0.

The rate of the species generation and depletion is described by the Arrhenius equation based on the law of mass action. The baseline result as the initial condition for the ablation simulation uses the 11-species model [2,3,7]. To facilitate a specific comparison for the phenolic–impregnated carbon ablator, the 18-species model by Olynick et al. [1] is adopted. The chemical species consist of CO_2, CO, N_2, O_2, NO, C_2, C_3, CN, H_2, HCN, C, N, O, H, C^+, N^+, O^+, and e^-. The chemical reactions involves nine dissociative, eight exchange, and three electronic impact processes. The detailed rate constants of the chemical kinetic model of Olynick et al. [1] are included in Table 1.

The internally consistent definition of the internal energy is now given as

$$\rho e = \sum_{i\neq e}\rho_i\left(c_{v,i}T + \frac{\mathbf{u}\cdot\mathbf{u}}{2}\right) + \sum_{i\neq e}\rho_e e_{v,i} + \sum_{i\neq e}\rho_i h_i^o + \rho_e\left(c_{v,e}T_e + \frac{\mathbf{u}_e\cdot\mathbf{u}_e}{2}\right) \tag{8}$$

where h_i^o is the standard heat of formation for all reacting species. In the absence of an externally applied electrical field, the electron drift velocity vanishes. The driven mechanism for electron motion is solely derived from diffusion; thus, the electron velocity can be calculated from Fick's law, like all neutral species in the high-temperature gas mixture [27].

The governing equation of spectral intensity for radiation is [4,24,25]

$$\mathbf{\Omega}\,\frac{\partial \mathbf{J}_\omega(\mathbf{r},\mathbf{\Omega})}{\partial r} + \kappa_\omega(\mathbf{r})\mathbf{J}_\omega(\mathbf{r},\mathbf{\Omega}) = j_\omega(\mathbf{r}) \tag{9}$$

where $\mathbf{J}_\omega(\mathbf{r},\mathbf{\Omega})$ is the spectral intensity of heat radiation; $\kappa_\omega(\mathbf{r})$ is the spectral absorption coefficient; and $j_\omega(\mathbf{r})$ is the spectral emission coefficient, which can be calculated in the condition of local thermodynamic equilibrium by the Kirchhoff law:

$$j_\omega(\mathbf{r}) = \kappa_\omega(\mathbf{r})J_{b,\omega}(\mathbf{r}) \tag{10}$$

The total radiation heat flux $\mathbf{q}_{\text{rad}}$ is obtained by integration over the radial $\mathbf{r}$ and solid angle $\mathbf{\Omega}$ through the full spectrum ω of the rotational line structure of diatomic and multi-atomic species. The radiative energy flux closes the system of equations for the global energy conservation equation (3):

$$q_{\text{rad}} = \int_{4\pi} \mathrm{d}\omega \int_{\Delta\omega_{\text{tot}}} J_\omega(\mathbf{r},\mathbf{\Omega})\Omega\,\mathrm{d}\Omega \tag{11}$$

In the present formulation for coupling of the radiative energy transfer, the radiative heat transfers is treated as a heat source or sink in the control volume of the interdisciplinary energy conservative equation. Therefore, the approach is different from that of Liu et al. [22], in which the NEQAIR is applied a posteriori after the flowfield has been determined. The coupling with the flowfield is explicitly and uniquely achieved iteratively through the nonequilibrium chemical species composition and thermodynamic states of the flow medium.

For the nonequilibrium hypersonic flow over a blunt body, the initial values and boundary conditions have been established [1–3]. The only implicit assumption for the species conservation equations at the surface is either noncatalytic or fully catalytic. However, the mostly widely used condition is simply to let the chemical reaction controls by the local thermodynamic condition identical to the interior domain [1–3,7–17]. Technically, it is assumed that the solid surface is catalytic. On the ablating surface, the interface boundary conditions are much more complex than the initial values [12–14]. The latter can be accurately described by the nonequilibrium, high-temperature air composition in the shock layer. In fact, some of the critical chemical reactions of the ablative material are exclusively determined by the components of the surrounding high-temperature air mixture [1,2,10–14]. For this reason, a detailed knowledge of the gas composition in the nonequilibrium shock layer and the physically meaningful interface boundary conditions are paramount in describing the ablation phenomenon. These initial values are provided by the numerical results, which are generated from the 11-species chemical kinetic model by Park [7].

Numerical Procedure

The system of governing equations including compressible aerodynamic, nonequilibrium chemical reactions, and spectral intensity equations is loosely coupled, but a uniform convergence criterion of the relative error is maintained for all numerical results on the order of magnitude of 10^{-5}. The interdisciplinary compressible aerodynamic equations; equations for momentum transfer were solved by a low-diffusion flux-splitting method through the time-derivative preconditioning to eliminate the numerical limiters [4,14,22]. The energy and species conservation equations are integrated by the implicit finite difference scheme of the second-order accuracy in space and time. The numerical stability for these

two groups of conservation equations can be easily maintained by treating the convective and diffusive terms by windward and central approximations, respectively. Finally, the radiative heat flux is generated by the multigroup spectral technique. The additional details of the adopted numerical procedures can be found in the work of Surzhikov et al. [6,18].

To be consistent with the kinetic models of internal structure of gas, transport properties of the gas mixture for thermal diffusion, viscosity, and thermoconductivity are calculated from Boltzmann equation by Chapman–Enskog expansion [27]. All collision integrals and cross sections are obtained from either the Lenard-Jones potential for nonpolar molecules or a polarizability model for ion-neutral nonresonant collisions by Capitelli et al. [28] and Levin and Wright [29] and augmented by the results by Svehla [30]. The kinetic theory also gives the viscosity and thermal conductivity for gas mixtures; these formulas are also known as Wilke's mixed rule [27].

The Stardust sample return capsule consists of a 60 deg one-half-angle spherical cone with a nose radius of 0.229 m as the forebody. The afterbody is a truncated 30 deg cone with a base radius of 0.406 m. The corner radius at the juncture the forebody and afterbody is merely 0.02 m [31]. At the peak heating condition of the forebody occurs at the reentry velocity of 11.137 km/s (altitude of 59.77 km) can be summarized as follows: the air density is 2.34×10^{-4} kg/m^3 and the ambient temperature is 238.5 K [1].

The entire flowfield is constructed by four contiguous domains, as displayed in Fig. 1. The near-body flowfield is described by three grid systems matched at the corners of the spherical cone forebody and the near-wake region. The first, second, and fourth grid blocks of the mesh have highly clustered grid spacing immediately adjacent to the surface of the capsule. The finest grid spacing of 0.01 cm is located on the fore face of the capsule. The far-field domain of the third grid block is overlaid on the near-wake grid block and the mesh density is highly stretched toward the far field downstream. The axisymmetric grid systems have the dimensions of 31×45, 31×27, 31×55, and 24×55. In the present analysis, the surface of the capsule is considered to be nonablative; thus, it is not necessary to assume a mass injection rate locally. To be compatible with the results of Olynick et al. [1], the Stardust sample return capsule surface is assumed to be fully catalytic. After the convergence of the initial solution on the coarse grid blocks, the final solution is repeated on the twice-refined grid cycle via a three-cycle, multigrid technique [15–17].

Conditions of Simulation

A total of five sequential computational simulations are performed during the reentry according to the time associated with the designed thermal protection trajectory of 42, 48, 54, 66 and 76 s after the atmospheric interface [31] (Table 2). These instants correspond to the altitudes of reentry at 71.92, 65.44, 59.77 51.19, and 46.51 km. The peak heating of the afterbody occurs at 66 s or the attitude of 51.19 km, at the same time the forebody also experiences the maximum surface pressure [1,31]. For the present study, all numerical simulations are approximated to have axisymmetric structure in facilitating the comparison with the benchmark results of Olynick et al. [1] and Park [2].

Table 2 Trajectory stages along the Stardust sample return capsule

Time, s	Altitude, km	ρ_∞, kg/m^3	ρ_∞, J/m^3	u_∞, m/s	T_∞, K
42	71.9	4.16×10^{-5}	2.640	12,413.4	221.4
48	65.4	1.06×10^{-4}	10.30	12,004.0	229.0
54 [a]	59.8	2.34×10^{-4}	16.00	11,136.7	238.5
66 [b]	51.2	7.21×10^{-4}	68.80	7,956.9	253.5
76	46.5	1.35×10^{-3}	123.00	5,178.9	256.9

[a]Peak forebody heating.
[b]Peak afterbody heating.

Figure 2 depicts the entire flowfield in a composite presentation of the static temperature and streamwise velocity component contours at the peak heating condition of the reentry trajectory, $t = 54$ s. The 11-species, finite rate chemical kinetic model for nonequilibrium air is used to establish the initial values for the ablation investigation [15]. After that, the 18-species chemical kinetic model for chemical reaction with carbonaceous surface by Olynick et al. [1] is applied, but without the active interaction with ablator. At the instant, the maximum postshock static temperature attains a value of 37,900 K, which is bracketed by a lower value of 24,000 K from the result of Olynick et al. [1] and a higher value of 58,600 K by Park [2]. Nevertheless, the attached strong bow shock and the rapid expansion around the corner of the forebody are accurately captured by the numerical simulation. The separated flow in the base region of the capsule correctly appears as a recirculating zone in the near wake. The secondary feature such as the neck of the near wake after the recompression for stream realignment is also exhibited. In short, all critical aerodynamic phenomena are reasonably duplicated.

Figure 3 depicts the species concentration in molar fractions within the shock envelope of the Stardust probe at the peak heating condition, $t = 54$ s. From this presentation; the bow shock standoff distance (1.3 cm) and the profiles of all chemical species agree very well with the result of Olynick et al. [1]. A high concentration of atomic nitrogen is observed in the stagnation region and extends to the outer edge of the heat shield. It becomes obvious that any chemical kinetic model does not include nitridation will under predict the mass blowing rate in the stagnation region where the dissociated nitrogen has a significant concentration [14,32]. Meanwhile, there is no significant presence of oxygen atoms adjacent to the ablator; the oxidation of carbon may have a limited effect on the ablation recession in the stagnation region. These important observations were first made by Chen and Milos [14] in their study on the thermal response of spacecraft heat shield for ablation phenomena.

The species concentration in molar concentration along the stagnation streamline at the later stage of the Stardust reentry,

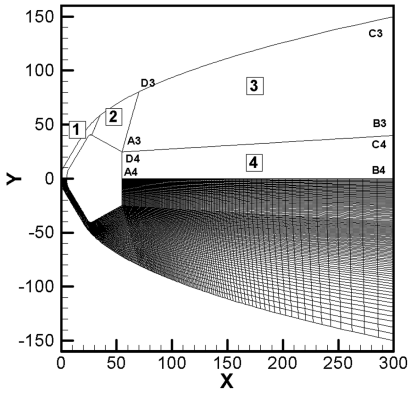

Fig. 1 Grid structure of Stardust return capsule flowfield 31×45, 31×27, 31×55, and 24×55.

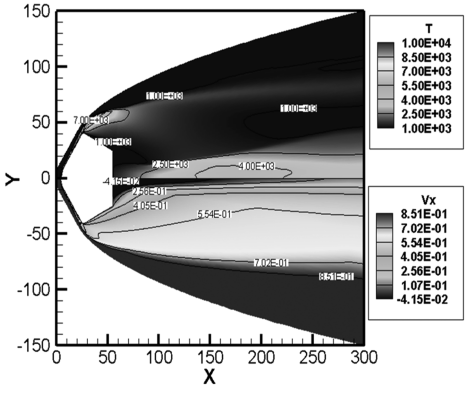

Fig. 2 Overall flowfield pattern (translational temperature and velocity) of reentering Stardust at $t = 54$ s, $T_\infty = 238.5$ K, and $V_\infty = 11.14$ km/s.

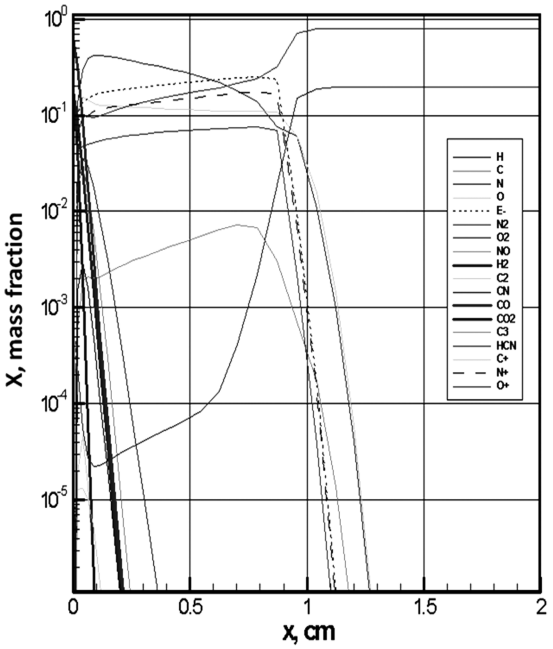

Fig. 3 Species molar fraction along stagnation streamline at $t = 54$ s, $T_\infty = 238.5$ K, and $\rho_\infty = 2.34 \times 10^{-4}$ kg/m^3.

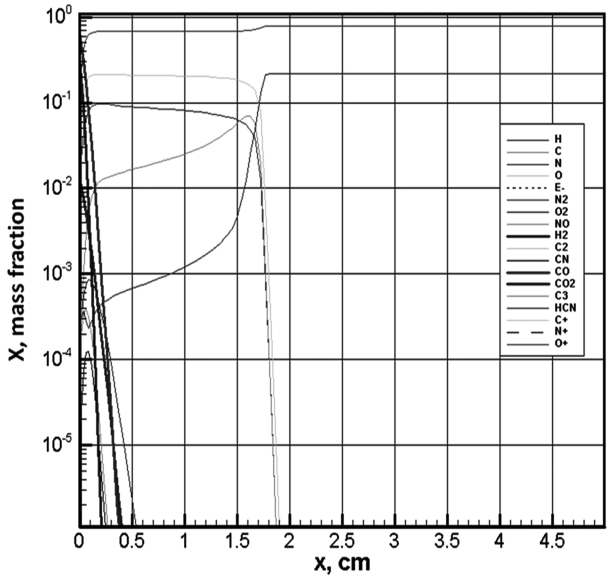

Fig. 4 Species molar fraction along stagnation streamline at $t = 75$ s, $T_\infty = 256.9$ K, and $\rho_\infty = 1.35 \times 10^{-3}$ kg/m^3.

$t = 76$ s, is presented in Fig. 4. The distribution of the species composition is very similar to that of the results obtained at previous time frames, but the standoff distance is substantiated increased to accommodate the changes in thermodynamic states and chemical species concentrations with respect to the altered condition of the shock layer and the freestream. At this instant, the atomic oxygen, nitrogen, and carbon are generated immediately downstream of the bow shock. The standoff distance is now increased to a value of 1.89 cm. As a reference for comparison, the asymptotic value of an ideal gas at the infinite Mach number is 3.82 cm. This behavior of gas mixture with excited internal degrees of freedom is significantly different from the perfect-gas medium to reflect the temporally complex nonequilibrium gas dynamic phenomena in reentry.

From the above numerical simulations at different stages of the reentry trajectory, the chemical composition and the distribution of internal degrees of energy have underwent a substantial adjustment to absorb, dissipate, and transmit the converted kinetic energy. The detailed energy state of the flow medium is delineated in the next section.

Internal Energy Transition

The complex ablative reentry phenomenon can be better understood by simultaneously examining the temporal events on the chemical composition and internal energy transfer in the shock layer over the forebody and the wake region during the process. For this purpose, the translational temperature of the gas mixture and vibrational temperatures of molecular nitrogen, oxygen, and nitric oxide in the shock layer are first presented in Fig. 5. The rotational temperatures of all chemical species are assumed to be equilibrated with translational mode and therefore will not be singled out in the discussion. The temperature distributions along the stagnation streamline from the marked time from 42 to 76 s are depicted together. The vibrational temperatures of chemical components are calculated from the internal energy of each species based on Maxwell–Boltzmann distribution. Under the thermodynamic nonequilibrium condition, the physical meaningfulness of these temperatures is challengeable, but it is adopted here as an approximation.

At the initial stage of reentry, most of the kinetic energy of the oncoming stream transfers into thermal energy to generate an aftershock maximum translational temperature up to 47,000 K. Shortly downstream of the bow shock, the vibrational temperatures of N_2, O_2, and NO reach a value of 11,000 K, which equals the translational temperature at a location of 0.60 cm downstream to the bow shock. The vibrational temperature of NO rises the fastest and follows in the order of N_2, and O_2, and these rates are persistent throughout all the cases studied. At a time elapsed of 6 s, more energy is transferred from translational to vibrational excitations; the maximum translational and the temperatures of vibrational mode also decrease to the values of 40,000 and 10,000 K, respectively. The thermal equilibrium condition of translational and vibrational excitation reaches at a downstream distance of 0.30 cm from the shock.

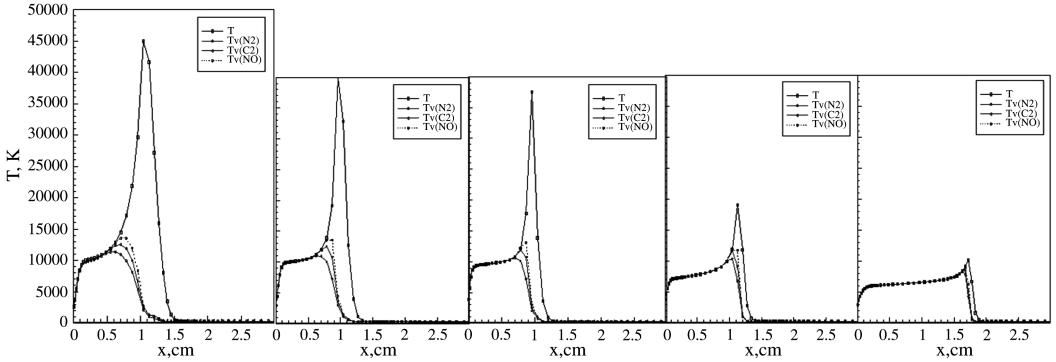

Fig. 5 Translational and vibrational temperature distributions along stagnation streamline; $42 < t < 76$ s, and $46.5 < \text{Alt} < 71.9$ km.

The persistently decreasing temperature of all internal modes indicates a portion of the thermal energy is transferring to the electronic excitation and radiation. However, the detailed mechanisms and what portion of it is redistributing to chemical kinetics of ionization are uncertain. Again, the electronic temperature is obtained by applied the Maxwell–Boltzmann distribution to the calculated electronic energy. From the solutions of the electronic energy conservation equation, Eq. (5) and earlier study [15]; the maximum electron temperature is 16,500 K and only exists in a short distance from the bow shock. The electronic temperature decreases rapidly as the ionized component moves away from the bow shock. From the computational results, the electronic temperature in the shock layer is around 10,000 K.

At the peak heating condition of the forebody, $t = 54$ s, the maximum translational and the temperature of the vibrational modes are 37,600 and 9800 K, respectively, within the shock layer. The thermal equilibrium condition of the translational and vibrational excitations occurs at a shorter distance of 0.25 cm downstream from the bow shock in comparison with the previous case. For the next simulation ($t = 66$ s), the standoff distance of the bow shock stays the same, but the thermal equilibrium condition is reached at an even shorter downstream distance from the shock by a value of 0.077 of the standoff distance. The maximum and the thermally equilibrium temperatures have reduced further to 20,000 and 8000 K, respectively.

At the last calculated trajectory point of $t = 76$ s, the peak translational temperature is further reduced to 11,000 K, and the temperatures of vibrational excitation attain the thermal equilibrium value with the translational mode at 7000 K. The thermally equilibrium condition is reached at a very short distance downstream from the bow shock like that of the previous case, but the standoff distance has increased to a value nearly of 2 cm, which is displayed in Fig. 5.

The significant difference in nonequilibrium temperatures patterns in the wake is highlighted by the temperature contours at $t = 42$, 54, and 76 s. In Fig. 6, the vibrational temperature of the molecular nitrogen is appended to the lower portion of the composite presentation together with the translational temperature. The maximum contour level of the temperature is reduced to 7000 K to an appropriately scaling to the lower nonequilibrium temperatures after expansion at the corner of the capsule.

First, at the initial reentry stage, $t = 42$ s, the nonequilibrium flow is extended to the far wake region. A high-vibrational-temperature region of molecular nitrogen follows the recompression of near wake in realigning the stream to the far wake. The vibrational energy of N_2 cascading to translational mode is also discernible as the resultant higher translational temperature diffuses from the axis of symmetry to the far field. The vibrational relaxation in the wake is characterized as a diffusion process rather than as the Landau–Teller process [3,4]. At the peak heating condition of the forebody, $t = 54$ s, the diffusion of the nonequilibrium vibrational temperature can still be observed as the elevated translation temperature is spreading from the axis of symmetry outward. The source of the diffused energy is derived from the deexcited vibrational degree of freedom. This phenomenon probably is unique for the nonequilibrium hypersonic flow over a blunt body. At the last simulation in time, $t = 76$ s, the thermal equilibrium condition between the translational and the molecular nitrogen vibrational mode has reached for the entire wake region.

A similar behavior is also observed for the vibrational temperatures of molecular oxygen and nitric oxide in the wake region; therefore, only two results near the initial stage of reentry ($t = 44$ s) and at the maximum afterbody heating load are depicted in Fig. 7. Again, the range of the temperature from 600 to 7000 K is depicted, and the vibrational temperature of the nitric oxide is appended to the lower portion of the composite presentation with the counterpart of molecular oxygen on top. At the initial stage, the vibrational temperature of NO is much higher than that of the O_2 and by a greater magnitude of 2170 K. The higher vibrational temperature of the nitric oxide concentration persists to a streamwise distances greater than two diameters of the capsule. It is interesting to note that the vibrational temperatures of O_2 and NO equilibrate in a shorter time period than that with the translational temperature. However, the

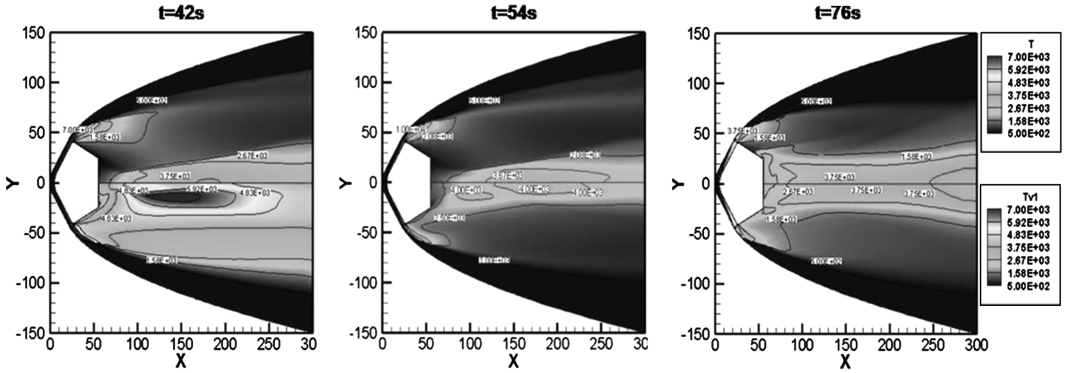

Fig. 6 Translational and vibrational temperatures of molecular nitrogen contours of Stardust reentry; $5.0 \times 10^2 < T$ and $Tv < 7.0 \times 10^3$ K.

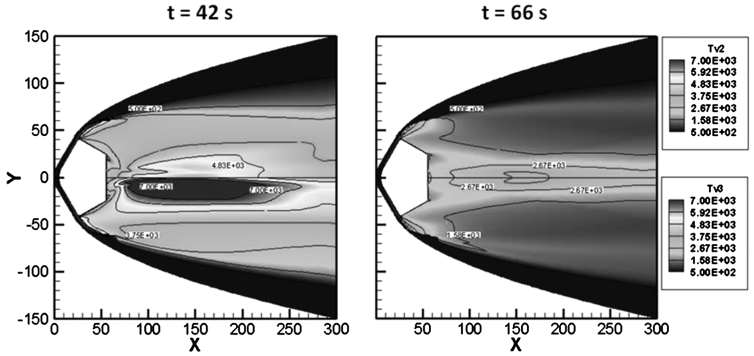

Fig. 7 Vibrational temperature of O_2 and NO contours at $t = 42$ and 66 s; $5.0 \times 10^2 < Tv < 7.0 \times 10^3$ K.

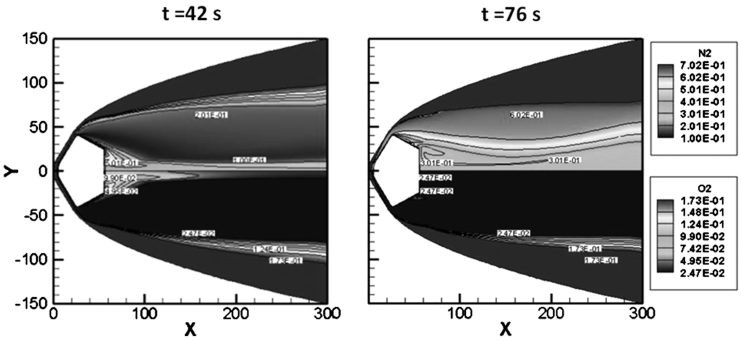

Fig. 8 Mass-fraction contours of molecular nitrogen ($0.100 < X_N < 0.702$) and oxygen ($0.0247 < X_O < 0.173\theta$).

precise rate of energy transfer among the two chemical species in reaching thermal equilibrium is unobtainable by the present simulation.

From the above simulations, it may be realized that the radiative energy transfer can have significantly different mechanisms from the initial stage in contrast to the later stage of reentry. At the early stage of reentry, the molecular vibrational excitation may first dominate the emission and absorption of photons, and then the electronic excitation becomes important near the peak heating condition. At the later stage of reentry, the deexcitation process in the shock layer is dominant by a lower energy state. In the wake region, the diffusive heat transfer plays an important role.

Species Concentration in Wake

From the combined experimental data of echelle spectrograph [33,34], the band heads of spectra of the first positive band of molecular nitrogen, the Schumann–Runge band of molecular oxygen, and the beta and gamma bands of nitric oxide, and the violet system of cyanide, CN, have been identified together with some metallic species. The emission bands of the atomic oxygen, O, and ionized nitrogen N_2^+ also have been detected. Since the optically active species control the photons emission, absorption, and propagation, the chemical composition around the Stardust is presented in this section. The chemical components in the shock layer of the forebody during the reentry are nearly invariant and only change in the layer thickness (Figs. 3 and 4). However, the wide variation is observed in the wake region and contributes to the radiative exchange.

Figure 8 presents the molecular mass fraction of the nitrogen (upper portion of the composite graph) and oxygen at the initial and the final stage of Stardust reentry, $t = 42$ and 76 s. The maximum contour level of the two species has assigned the different values according to its unperturbed fraction in the freestream. At the early stage of reentry, both the molecular components are substantially depleted. The mass fraction of the N_2 has been reduced to the value of 0.201, and O_2 also reached a lower value of 0.0247. However, a strong recombination process takes place at the outer corner of the afterbody for bother the molecular species to recover to almost its unperturbed freestream value locally.

At the final reentry stage, $t = 76$ s, the depleted molecular oxygen in mass fraction retains a constant value of 0.0247 throughout the entire wake region. The molecular nitrogen is nearly completely recombined in the outer portion of the wake toward the shock envelope, but is depleted to half of the unperturbed freestream value in the inner core of the wake. The released heat of formation will contribute to the diffusive heat transfer in the wake.

The mass fractions of the atomic nitrogen and oxygen span a wider range in the initial and the final stage of the reentry and therefore have to be depicted in different contour levels. The mass fractions of atomic nitrogen and oxygen at initial stage, $t = 42$ s, are presented in Fig. 9. The range of the mass fraction of N is from 0.0246 to 0.172, the counterpart of O is from 0.0268 to 0.195. The outstanding feature through the recombination process is depicted for both species in the base region of the capsule. The atomic species reach their lowest concentration in the recirculating zone.

The mass-fraction contours of the atomic species of nitrogen and oxygen at $t = 76$ s are presented in the same composite format in Fig. 10. In this figure, the contours of N are scaled in the range from 0.0236 to 0.165, and the contours of O range from 0.0407 to 0.285. The variation of the concentration of N is smaller in comparison with the concentration of O. The former displayed a nearly uniform value of 0.472 over the entire wake region. On the other hand, the concentration of the atomic oxygen reveals a slightly greater variation than the atomic nitrogen, but the change is less than 18%.

The concentrations of cyanide, CN, and ionized molecular nitrogen appear only as trace elements of the gas mixture, and the latter is included in the 18-species chemical kinetics model [1]. The important observation from the species concentration over the entire flowfield is that the radiative energy transfer is closely associated with the atomic and molecular nitrogen and oxygen. Meanwhile, the nitrogen and oxygen recombination process contributes to the increasing diffusive heat transfer at the later stage of the Stardust reentry.

Radiative Heat Exchange

The numerical methods for simulating radiative flux are the multigroup spectral models, including the wide- and narrowband spectral models, and the line-by-line integration over the investigated spectrum. All these computational approaches are actually very similar; a studied spectral range is divided into a finite numbers of spectrum domains. In the limit, the spectral intensity equation (9) is solved with a frequency-independent coefficients of emission and absorption in the divided spectrum bands. The radiative energy flux is obtained by integrating over the complete spectrum [24,25]. The complication of nonlinear line structure of the spectra along the optically thick path is also bypassed by an averaged linear structure of atomic and molecular spectra. In a reduced dimensional approximation, the half-moment method by Sherman [35] has demonstrated to be the best approach to solve the loosely coupled radiative gas dynamics problem [24].

From the calculated radiative fluxes on the capsule surface and the spectral absorption coefficients near the surface, a shifting in wavelength or frequency corresponding to the different times of the

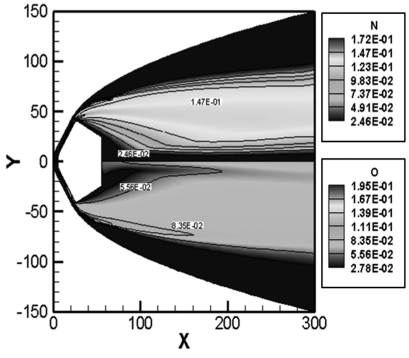

Fig. 9 Mass-fraction contours of atomic nitrogen ($0.0246 < X_N < 0.172$) and oxygen ($0.0278 < X_O < 0.195$) at $t = 42$ s.

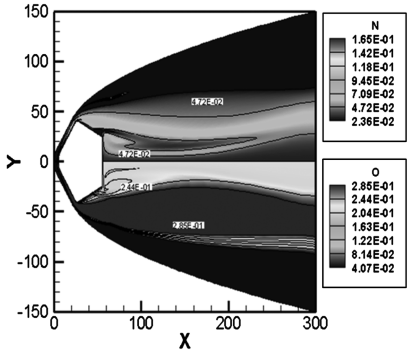

Fig. 10 Mass-fraction contours of atomic nitrogen ($0.0236 < X_N < 0.165$) and oxygen ($0.0407 < X_O < 0.285$) at $t = 76$ s.

reentry is revealed. The shifted wavelength domain of emission and absorption indicates the changing of the originating optically active species and their excited states. As described in the previous sections, these patterns are closely tied to the species compositions and energy states of various internal degrees of freedom in the shock layer. Figure 11 depicts the radiative heat fluxes with respect to the wave number (frequency) at four trajectory points ($t = 48$, 54, 66, and 76 s). The active emission is concentrated around the wave number from 10^4 to 10^5/cm, which corresponds to the wavelength from 1000 to 100 nm. This wide range of wavelengths or spectra contains the Schumann–Runge band of O_2 the β and γ systems of NO, the first and second positive of N_2, the fourth positive band of CO, and the violet and red systems of CN. Some ionized species may also include the first negative band of O_2^+, as well as the first negative N_2^+ band, but it cannot be clearly identified. All radiative exchanges are resolved by 200,000 spectral points in the present computations.

In Fig. 12, the radiative heat fluxes on the surface are depicted for $t = 48$ and 76 s, which represented the intensity of radiative energy emission in time over the spectral measured by wave number from 10^3/cm to 2.0×10^5/cm. These frequencies correspond to a wavelength range from 10,000 to 196 nm. At the earlier stage of reentry, the high intensity of surface radiative flux is concentrated in the upper range of 10^4/cm to 2.0×10^5/cm and shifts toward the middle-wave-number range. This lower-wave-number range contains the first positive band of nitrogen (740–870 nm), Schumann–Rung system of oxygen (780–850), and the violet system of CN (386–421.5 nm). The radiative emissions in this spectrum have been detected by the measurements using an echelle spectrograph [33,34]. The atomic nitrogen N and oxygen O, in fact, have lines and multiples (80-1, 400 nm) at the higher wave number range up to 1.25×10^5/cm. The radiative energy exchange in the studied spectrum remains similar and sustained from the time from $t = 48$ until 66 s, including the peak heat transfer condition of the forebody of the Stardust capsule, $t = 54$ s.

At the later stage of reentry, $t = 76$ s, the radiative heat flux on the surface decreases over the entire studied spectral. In the lower-wave-number domain from 10^3/cm to 10^4/cm, the magnitude of intensity reduces by nearly two orders of magnitude. The radiation heat transfer ceases beyond the spectral value of 10^5/cm. The downward shift of radiative wave number is reflected by the lower temperature in the shock layer according to the Wien displacement law for spectral energy density function [4,24].

The spectral absorption coefficients near the surface of Stardust capsule for the times from 48 to 76 s are presented in Fig. 13. The radiative energy transfer is calculated based on the local flowfield condition to show the dependence of radiative intensity to the propagating medium. The displayed absorption coefficients consist of two results generated at the local (within boundary layer) and the maximum near-surface (in shock layer) temperature of the Stardust capsule to reflect the influence of the near-surface temperature of the emitter. At the initial and the maximum forebody heating condition, $t = 54$ s, the calculated spectral range of absorption coefficient in terms of wave number is from 10^4/cm to 1.8×10^5/cm. All the absorption coefficients have a similar pattern; the high absorption coefficients on the surface is clustered near the middle range of wave number from 5.0×10^4/cm to 1.2×10^5/cm, and a spike domain is centered around 2.0×10^4/cm. The difference between absorption based on local surface and maximum near-surface temperature is noticeable in the spectral domain from low (3.0×10^4/cm) to middle (5.0×10^4/cm) range.

At $t = 66$ s, the absorption coefficients on the surface of the forebody are present in the range from 10^4/cm to 10^5/cm. The spike of coefficient distribution is still apparent at the wave number of

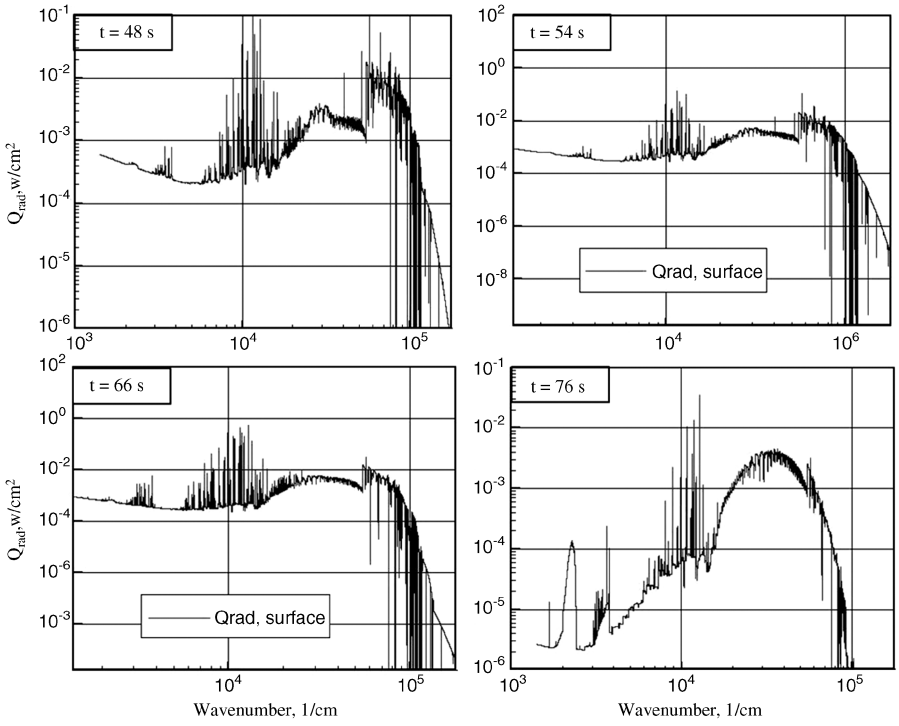

Fig. 11 Spectral of radiation transfer from the Stardust forebody.

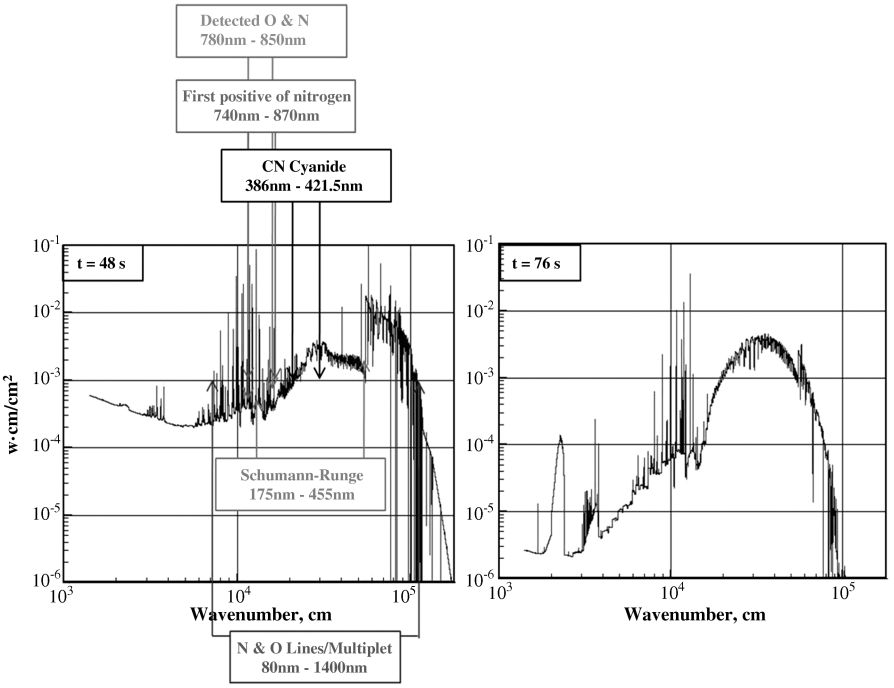

Fig. 12 Radiation heat flux on the surface of Stardust.

2.0×10^4/cm. The discrete absorption coefficients of spectral lines are detected beyond the wave number of 5.5×10^4/cm. Finally, the results at $t = 76$ s are given in the spectral range of 10^3/cm to 2.0×10^5/cm. The absorption coefficients indicate spectral intensity centered on the wave number of 10^4/cm and 10^5/cm. The difference between coefficients of the local and maximum near-surface temperature is very pronounced. This discrepancy can be understand in which the maximum near-surface temperature in the shock layer is the highest at the initial reentry stage and decreases steadily in time, as shown in Fig. 5. Therefore, it may not be an accurate calculation by a fixed reference for surface absorption coefficient computation. At the same time, the accurate near-surface temperature is shown to be paramount for predicting the emission and absorption of radiative heat transfer.

Heat Transfer Rate

The total heat transfer to the Stardust consists of the components of conductive, diffusive, and radiative mechanisms. In the present investigation, the interactions of the ablator charring and pyrolysis

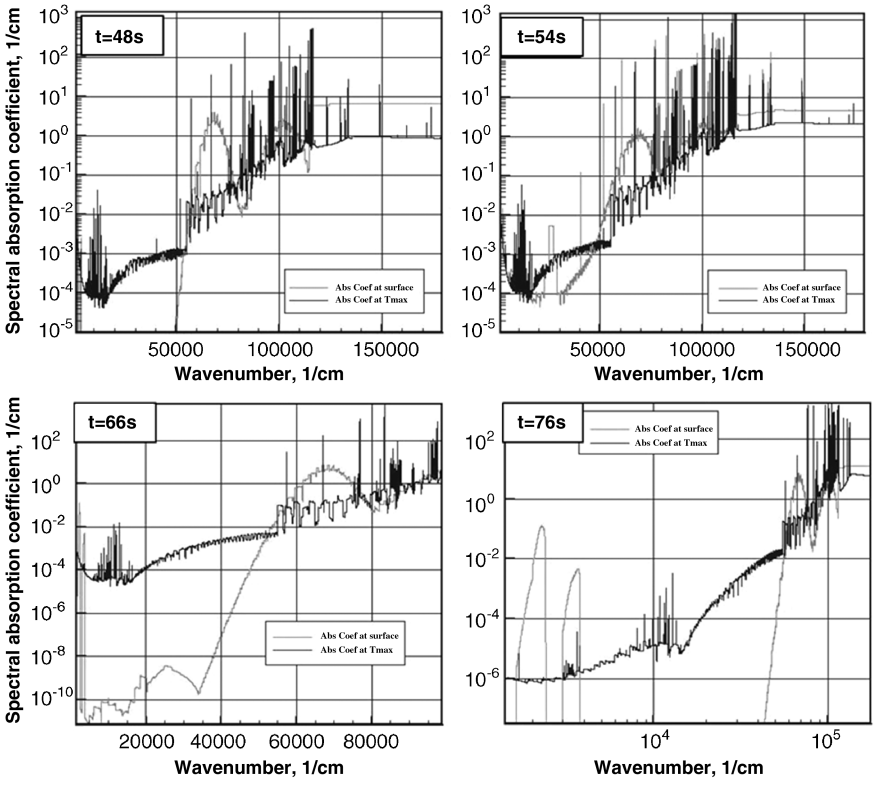

Fig. 13 Surface and near-surface spectral absorption coefficients in shock layer.

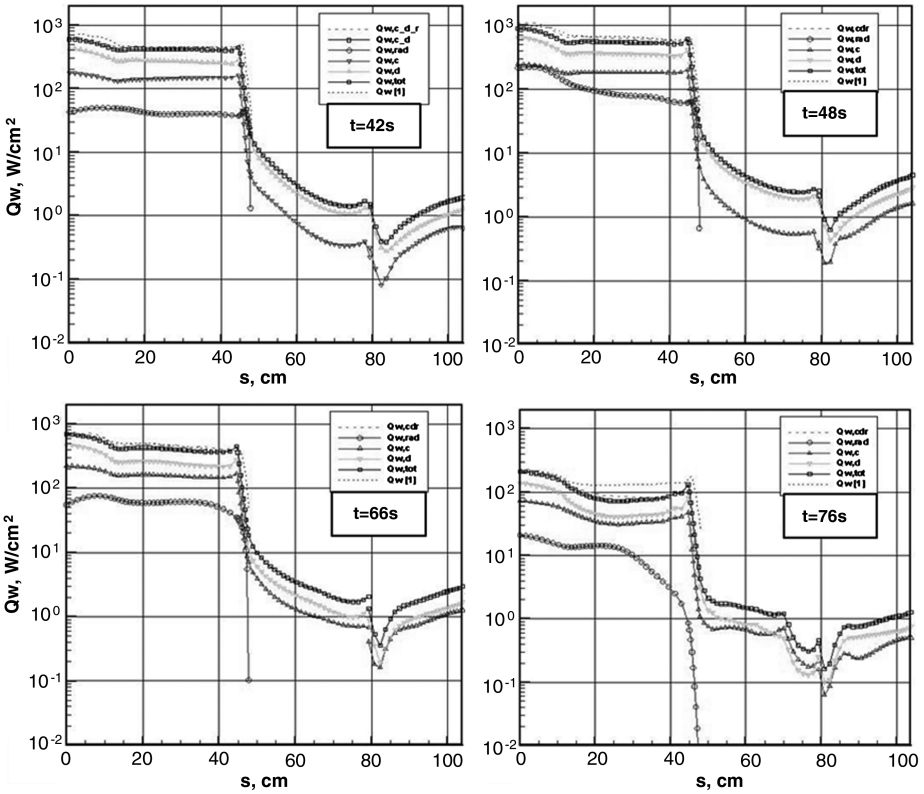

Fig. 14 Heat transfers along the symmetric plane of Stardust capsule; 42 s $< t <$ 76 s.

gas interaction with external flow have not been taken into consideration. Therefore, the surface blowing contribution to ablation cooling is not addressed. The comparison with the results of Olynick et al. [1] is therefore limited to the nonablating condition.

The heat transfer rates to the Stardust capsule are first presented before and after the maximum heating load condition on the forebody in Fig. 14. The heat transfer distributions are recorded for the time frames of 42, 48, 66, and 76 s. Before the peak heating load at the forebody, the diffusive heat transfer increases with time, in direct contrast to the deceasing contribution by conduction to the total heat transfer rate. This behavior is in good correlation with the deceasing aftershock temperature in time, as revealed in Fig. 5. The radiative heat transfer has order-of-magnitude increases from 44 to 205 W/cm^2 in the early stage of reentry and then decreases to a value less than 20 W/cm^2 toward the later stage of reentry. The present results indicate a rate similar to those of Olynick et al. [1] and Park [2]. The radiative heat transfer is rather uniformly distributed over the entire front surface of the forebody, except at the last stage, $t = 76$ s. At that instant, the radiative energy exchange is reduced toward the corner of the capsule. Overall, the total heat transfer rate without active ablating interaction has a range from 200 to over 1020 W/cm^2, to agree with most computational simulations [1,2,10–14]. The present simulation also provides interesting heat transfer information in the wake region. From $t = 42$ s onward, the diffusive heat transfer begins to increase when the recombination process of atomic nitrogen and oxygen takes place as the nonequilibrium gas mixture exits the downstream computational domain.

After the peak heating load is reached, the diffusive heating increases at $t = 66$ s, not only in the forebody, but also in the near wake. The heat release by the deexcited molecular nitrogen from its vibrational mode and the recombination heat of formation of nitric oxide are identified as the energy source for the observed higher diffusive heat transfer rate. The internal energy transfer processes are shown in Figs. 6 and 7. In essence, the wake region is strongly affected by the heat release from the relaxation of the vibrational and electronic excitations. In general, the present results of heat transfer rate agree very well with the computational solutions by Olynick et al. [1], including the radiative heat transfer, and reach an excellent agreement at the last reentry stage simulated. Unfortunately, there are no results in the wake region for the purpose of comparison and verification.

The heat transfer rate at the peak heat load condition of the forebody is presented in Fig. 15. The conductive heat transfer contributes a value of 320 W/cm^2 to the total heat transfer rate at the stagnation point. The combined conductive and diffusive heat transfer rates yield a value of 1.19×10^3 W/cm^2 at the stagnation point of the capsule. The present total heat transfer rate without active ablation is in a very good agreement with the nonablating results by Olynick et al. [1] of 1.2×10^3 W/cm^2 and agrees equally well with the laminar flow result of Park [2] at 1.189×10^3 W/cm^2. The radiative heat transfer rate over the forebody, however, reveals a value of 248 W/cm^2, comparable with the results by Olynick et al. [1] and

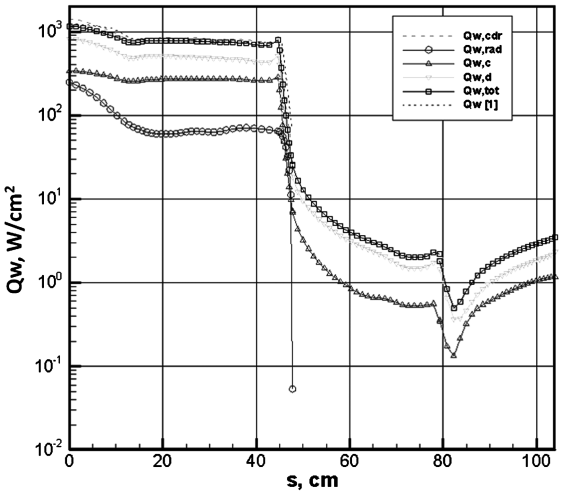

Fig. 15 Heat transfer rate at peak heating condition along the symmetric plane of Stardust capsule.

Park [2]. Overall, the present radiative heat transfer indicates a mostly constant rate over the frontal face of the Stardust capsule that drops sharply at the juncture of the forebody and afterbody of the capsule, similar to that of Olynick et al. [1] At the same instance, the diffusive heating in the wake region begins to rise through energy cascading from vibrational excitation and chemical species recombination as the nonequilibrium flow leaves the computational domain.

Conclusions

The radiative heat transfer using multigroup spectral approximation is integrated with the interdisciplinary formulation for nonequilibrium hypersonic flow. The developed computational capability successfully simulates the reentry of the Stardust sample return capsule at difference instants along its trajectory. The radiative heat transfer to the forebody of the Stardust capsule is generated by using the multigroup method. The predicted total heat transfer rates without an active ablative surface interaction agree very well with the nonablating results.

The dominant emission spectrum of radiative from the computational result correlates very well with the echelle spectrograph findings, and the result also verifies the time-dependent internal degree of excitation and relaxation of the gas medium during the reentry. The observed wave number shifting in the radiative intensity also correctly follows the Wien displacement law for spectral energy density function.

Finally, the simulated flowfield around the reentry capsule reveals that the relaxation extends beyond the shock layer into the wake region. The computational simulations show explicitly that the recombination and deexcitation of electronic and vibrational mode generate a higher diffusive heat transfer in the wake region.

Acknowledgments

The authors deeply appreciate the sponsorship by John Schmisseur of the U.S. Air Force Office of Scientific Research and the support by Donald Paul and Jose Camberos of the U.S. Air Force Research Laboratory through the Summer Visiting Scholar program.

References

[1] Olynick, D., Chen, Y.-K., and Tauber, M. E., "Aerothermodynamics of the Stardust Sample Return Capsule," *Journal of Spacecraft and Rockets*, Vol. 36, No. 3, 1999, pp. 442–462. doi:10.2514/2.3466

[2] Park, C., "Calculation of Stagnation-Point Heating Rates Associated with Stardust Vehicle," *Journal of Spacecraft and Rockets*, Vol. 44, No. 1, 2007, pp. 24–32. doi:10.2514/1.15745

[3] Park, C., "Review of Chemical-Kinetic Problems of Future NASA Mission, I: Earth Entries," *Journal of Spacecraft and Rockets*, Vol. 7, No. 3, 1993, pp. 385–398. doi:10.2514/3.431

[4] Zel'dovich, Ya. B., and Raizer, Yu. P., *Physics of Shock Waves and High-Temperature Hydrodynamic Phenomena*, Dover, Mineola, NY, 2002, pp. 107–348.

[5] Laux, C. O., Winter, M., Merrifield, J., Smith, A., and Tran, P., "Influence of Ablation Products on the Radiation at the Surface of a Blunt Hypersonic Vehicle at 10 km/s," AIAA Paper 2009-3925, San Antonio, TX, 2009.

[6] Surzhikov, S. T., Sharikov, I. V., Capitelli, M., and Colonna G., "Kinetic Models of Nonequilibrium Radiation of Strong Air Shock Waves," AIAA Paper 2006-0586, 2006.

[7] Park, C., "Chemical-Kinetic Parameters of Hypersonic Earth Entry," *Journal of Thermophysics and Heat Transfer*, Vol. 15, No. 1, 2001, pp. 76–90. doi:10.2514/2.6582

[8] Zhong, J., Ozawa, T., and Levin, D. A., "Modeling of Stardust Reentry Ablation Flows in the Near Continuum Flight Regime," *AIAA Journal*, Vol. 46, No. 10, 2008, pp. 2568–2581. doi:10.2514/1.36196

[9] Boyd, I. D., Zhong, J., Levin, D. A., and Jenniskens, P., "Flow and Radiation Analyses for Stardust Entry and High-Altitude," AIAA Paper 2008-1215, Reno, NV, 2008.

[10] Cheatwood, F., and Gnoffo, P., "User's Manual for the Langley Aerothermodynamic Upwind Relaxation Algorithm (LAURA)," NASA TM 4674, April 1996.

[11] Wright, M. J., Candler, G. V., and Bose, D., "Data-Parallel Line Relaxation Method for the Navier-Stokes Equations," *AIAA Journal*, Vol. 36, Sept. 1998, pp. 1603–1609. doi:10.2514/2.586

[12] Milos, F., and Chen, Y., "Ablation And Thermal Response Property Model Validation for Phenolic Impregnated Carbon Ablator," AIAA Paper 2009-0262, Orlando FL, 2009.

[13] Chen, Y. K., and Milos, F. S., "Navier-Stokes Solutions with Finite Rate Ablation for Planetary Mission Earth Mission Earth Reentries," *Journal of Spacecraft and Rockets*, Vol. 42, No. 6, 2005, pp. 961–970. doi:10.2514/1.12248

[14] Chen, Y. K., and Milos, F. S., "Ablation and Thermal Response Program for Spacecraft Heat Shield Analysis," *Journal of Spacecraft and Rockets*, Vol. 36, No. 3, 1999, pp. 475–483. doi:10.2514/2.3469

[15] Shang, J. S., and Surzhikov, S. T., "Simulating Nonequilibrium Flow for Ablative Earth Reentry," *Journal of Spacecraft and Rockets*, Vol. 47, No. 5, 2010, pp. 806–815. doi:10.2514/1.49923

[16] Shang, J. S., Surzhikov, S. T., and Yan, H., "Simulating Hypersonic Nonequilibrium Flow Using Kinetic Models," AIAA Paper 2009-0286, Orlando, FL, 2009.

[17] Shang, J. S., "Analysis of Hypersonic Nonequilibrium Flow over Ablating Surface," AIAA Paper 2009-4051, San Antonio, TX, 2009.

[18] Surzhikov, S. T., and Shang, J. S., "Kinetics Models Analysis for Super-Orbital Aerophysics," AIAA Paper 2008-1278, Reno, NV, 2008.

[19] Treanor, C. E., and Marrone, P. V., "Effect of Dissociation on the Rate of Vibrational Relaxation," *Physics of Fluids*, Vol. 5, No. 9, 1962, pp. 1022–1026. doi:10.1063/1.1724467

[20] Kudryavtsev, N. N., Kuznetsova, L. A., and Surzhikov, S. T., "Kinetics and Nonequilibrium Radiation of CO2-N2 Shock Waves," AIAA Paper 2001-2728, Anaheim, CA, 2001.

[21] Olynick, D. R., Henline, W. D., Chambers, L. H., and Candler, G. V., "Comparison of Coupled Radiative Navier-Stokes Flow Solutions with the Project Fire-II Flight Data," AIAA Paper 94-1955, 1995.

[22] Liu, Y., Prabhu, D., Trumble, K. A., Saunders, D., and Jenniskens, P., "Radiation Modeling for the Reentry of the Stardust Sample Return Capsule," *Journal of Spacecraft and Rockets*, Vol. 47, No. 5, 2010, pp. 741–752. doi:10.2514/1.37813

[23] Whiting, E. E., Park, C., Liu, Y., Arnold, J. O., and Paterson, J. A., "NEQAIR96, Nonequilibrium and Equilibrium Radiative Transport and Spectral Program: User Manual, NASA Rept. 1389, Dec. 1966.

[24] Surzhikov, S. T., "Computing System for Solving Radiative Gasdynamic Problems of Entry and Re-Entry Space Vehicles," *Proceedings of the International Workshop on Radiation of High Temperature Gases in Atmospheric Entry*, SP-533, ESA, 8–10 Oct. 2003, pp. 111–117.

[25] Surzhikov, S. T., "Radiation Modeling and Spectral Data," *Physico-Chemical Models for High Enthalpy and Plasma Flows*, Lecture Series 2002–07, von Karman Inst. for Fluid Dynamics, Rhode-Saint-Genèse, Belgium, 2002.

[26] Vincent, W. G., and Traugott, S. C., "The Coupling of Radiative Transfer and Gas Motion," *Annual Review of Fluid Mechanics*, Vol. 3, 1971, pp. 89–116. doi:10.1146/annurev.fl.03.010171.000513

[27] Bird, R. B., Stewart, W. E., and Lightfoot, E. N., *Transport Phenomenon*, 2nd ed., Wiley, New York, 2002, pp. 25, 274, 526.

[28] Capitelli, M., Gorse, C., Longo, S., and Giordano, D., "Collision Integrals of High-Temperature Air Species," *Journal of Thermophysics and Heat Transfer*, Vol. 14, No. 2, 2000, pp. 259–268. doi:10.2514/2.6517

[29] Levin, E., and Wright M. J., "Collision Integrals for Ion-Neutral Interactions of Nitrogen and Oxygen," *Journal of Thermophysics and Heat Transfer*, Vol. 18, No. 1, 2004, pp. 143–147. doi:10.2514/1.2552

[30] Svehla R. A., "Estimated Viscosities and Thermal Conductivities of Gases at High Temperatures," NASA TR-R-132, 1962.

[31] Desai, P. N., Lyons, D. T., Tooley, J., and Kangas, J., "Entry, Descent, and Landing Operations Analysis for The Stardust Entry Capsule," *Journal of Spacecraft and Rockets*, Vol. 45, No. 6, 2008, pp. 1262–1268. doi:10.2514/1.37090

[32] Zhluktov, S., and Abe, T., "Viscous Shock-Layer Simulation of Air Flow Past Ablating Blunt Body with Carbon Surface," *Journal of*

Thermophysics and Heat Transfer, Vol. 13, No. 1, 1999, pp. 50–59. doi:10.2514/2.6400

[33] Jenniskens, P., "Observations of the Stardust Sample Return Capsule Entry with a Slit-Less Echelle Spectrograph," AIAA Paper 2008-1210, Reno, NV, Jan. 2008.

[34] McHarg, M. G., Stenbaek-Nielsen, H. C., and Kanmae, T., "Observations of the Stardust Sample Return Capsule Entry Using a High Frame Rate Slit-Less Echelle Spectrograph," AIAA Paper 2008-1210, Reno, NV, Jan. 2008.

[35] Sherman, M. P., "Moment Methods in Radiative Transfer Problem," *Journal of Quantitative Spectroscopy and Radiative Transfer*, Vol. 7, 1967, pp. 89–109.

G. Palmer
Associate Editor